AIAA SciTech Forum
8-12 January 2024, Orlando, FL
AIAA SCITECH 2024 Forum

10.2514/6.2024-1384

Unsteady Swirl Distortion in a Short Intake Under Crosswind Conditions

Tommaso Piovesan[1], Pavlos K Zachos[2] and David G MacManus[3]

School of Aerospace, Transport and Manufacturing, Cranfield University, Cranfield, UK

Christopher Sheaf [4]

Rolls-Royce plc., Derby, UK

In crosswind operating conditions, an aero-engine intake can be affected by notable unsteady flow distortions at the fan face. These distortions are typically associated with the ingestion of the ground vortex as well as with flow separation within the intake and can have a detrimental effect on the intake performance and therefore on the operability of the downstream compression system. Measurements of the unsteady velocity field within a model-scale intake under crosswind conditions were conducted using Stereo Particle Image Velocimetry (S-PIV) to characterize the velocity field and hence the intake flow distortion across the Aerodynamic Interface Plane (AIP) inside the duct. The intake distortion metrics were calculated for three operating conditions at a fixed crosswind velocity and increasing Mass Flow Capture Ratio (MFCR). The conditions at which the flow separates depend on crosswind velocity, ground clearance, the design of the intake and the MFCR. Flow characteristics of both low MFCR diffusion-driven, and high MFCR shock-induced separation were identified. The circumferential extent and intensity of the swirl distortion were found to be highly dependent on the crosswind velocity and MFCR. The swirl distortion caused by the diffusion-driven separation is greater than that due to shock-induced separation. The diffusion-driven separation was found to affect a bigger position of the intake AIP with higher time-average and peak values. An intermittent separation, that was observed for one value of MFCR in the range investigated, was found to cause peak levels of distortion twice the time-averaged values. Localized high swirl levels at a radial position near the intake surface correspondent to the tip region of a notional fan were observed. These can be expected to be detrimental to the operating stability of the downstream compression system.

I. Nomenclature

$\tilde{\dot{m}}$	=	corrected intake mass flow rate, kg/s
$\dot{m}$	=	intake mass flow rate, kg/s
A_{hi}	=	highlight area, m^2
AIP	=	Aerodynamic Interface Plane
D_{hi}	=	highlight diameter, m
D_i	=	intake inner diameter, m

[1] Doctoral Researcher, Centre for Propulsion and Thermal Power Engineering.
[2] Reader in Propulsion Aerodynamics, Centre for Propulsion and Thermal Power Engineering, AIAA Member.
[3] Professor in Propulsion Aerodynamics, Centre for Propulsion and Thermal Power Engineering, AIAA Member.
[4] Cold End Centre of Excellence, Installation Aerodynamics Specialist, Rolls-Royce plc.

h	=	vertical distance from lowest point of the highlight plane to ground, m
L_i	=	intake length, m
$MFCR$	=	Mass Flow Capture Ratio
M_{is}	=	isentropic Mach number
$P_{0,\infty}$	=	freestream total pressure, Pa
r	=	radius, m
R_{AIP}	=	AIP radius, m
Re	=	Reynolds number
SC	=	Swirl Coefficient
SD	=	Swirl Directivity
SI	=	Swirl Intensity, deg
T	=	static temperature, K
$T_{0,\infty}$	=	freestream total temperature, K
u, v, w	=	cartesian instantaneous velocities, m/s
U, V, W	=	cartesian area averaged time averaged velocity components, m/s
V_∞	=	freestream velocity, m/s
W, V_θ, V_r	=	cylindrical area averaged time averaged velocity components, m/s
$w, v_\theta, v_r,$	=	cylindrical instantaneous velocities, m/s
x, y, z	=	cartesian frame of reference
x, θ, r	=	cylindrical frame of reference
α	=	swirl angle, degrees
μ	=	dynamic viscosity, kg/ms
ρ_∞	=	freestream density, kg/m^3

II. Introduction

The next generation of turbofan aeroengines will feature increased fan diameters to reduce fuel consumption and increase overall efficiency ([1]-[3]). To reduce weight and drag, more compact nacelles featuring shorter intakes may be used to maximize the performance contributing to future environmental targets. In contrast to conventional intakes, short intakes may feature reduced internal diffusion capabilities and non-negligible interaction with the downstream fan [4]. Therefore, short intakes could be more susceptible to generating more complex flow distortion, especially under off-design operating conditions, such as in presence of crosswind. The performance of short intakes close to the ground in presence of a crosswind can be strongly affected by multiple sources of distortion, including the presence of an ingested vortex originating from the ground and by the flow separation which arises on the windward side inside the intake.

The characterization of the ground vortex has been the focus of different experimental and computational studies over the past decades. Initial studies focused on the formation mechanisms ([5]-[7]) and their relations with the operating points and geometric parameters of the intake ([8]-[10]). More recently, Murphy et al. [11] and Wang and Gursul [12] focused on the unsteady aspects of the ground vortex in terms of strength and size on measurements planes underneath and in front of the intake using Particle Image Velocimetry (PIV). However, the swirl distortion caused by the ingested vortex on a nominal Aerodynamic Interface Plane (AIP) inside the intake was not measured.

The intake flow separation has been primarily investigated at high angles of attack, both experimentally ([13]-[17]) and numerically ([18]-[21]). Recent experimental ([22]-[25]) and numerical ([26]-[28]) studies have documented the different features of the intake separation under crosswind conditions, which depend on the intake mass flow and on the magnitude of the crossflow. With a constant crosswind velocity, the intake flow encompasses three different regimes, that is low-speed or diffusion-driven separation, attached condition, and shock-induced separation, as illustrated in Fig. 1.

The investigations cited previously, both experimental and numerical, were performed either with intrusive measurement techniques with low temporal and spatial resolution, or with steady state simulations, which do not capture the unsteadiness of the separated intake flow. Unsteady distortion and peak instabilities can severely worsen the performance of the intake ([29]) and the coupled effect of both total pressure distortion and swirl distortion, due to the presence of the ground vortex and the separated flow, can affect the operability margin of the intake-fan-system more than with time-averaged total pressure distortion acting alone ([30]).

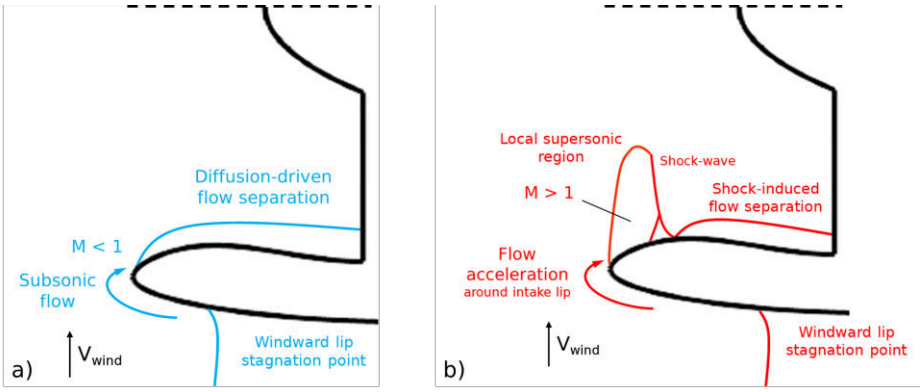

Fig. 1 Flow features within an intake under crosswind: a) diffusion-driven separation; b) shock-induced separation.

In this paper, the evaluation of the unsteady swirl distortion associated with distorted velocity flow fields inside an intake in crosswind at different operating conditions is performed. The swirl distortion is assessed and quantified by using PIV measurements on a typical Aerodynamic Interface Plane (AIP) inside the intake, calculating both the time-averaged values and the unsteady variations. Focusing on the two main mechanisms of separation inside an intake in crosswind conditions, i.e. diffusion-driven separation and shock-induced separation, and on the ingested ground vortex, this work provides insights on the relationship between these flow mechanisms and the amount of distortion, which is of key importance in the assessment of the intake performance and the impact on the downstream compression system.

III. Experimental Setup and Data Analysis Methodology

A. Experimental Facility and Intake Model

The experiments were conducted at the Low-Speed Tunnel of the German-Dutch Wind Tunnels (LST-DNW). The LST-DNW is a continuous, atmospheric, low-speed wind tunnel, with a 3.022 x 2.25 m^2 test cross section and a maximum achievable tunnel velocity (in empty conditions) of 80 m/s. A test rig was designed to accommodate an intake model with ground plane to mimic ground operations. A schematic of the wind tunnel's working section is shown in Fig. 2.

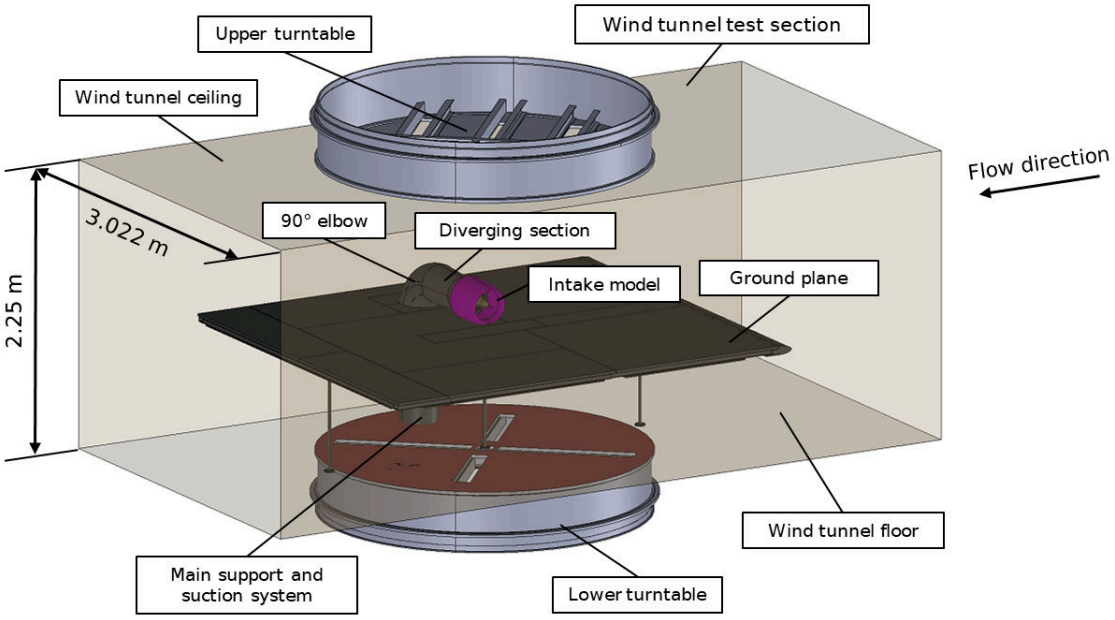

Fig. 2 Schematic of the LST-DNW wind tunnel test section.

The intake model was located at the center of the test section and mounted on a 90-degree-bent duct with a diverging section, which served both as suction system and as model support. A set of 4 suction pumps was used to drive the air flow through the intake model. The model and the suction pipe were placed on the LST floor turntable and oriented perpendicular to the incoming flow to reproduce crosswind conditions. The ground plane had an elliptical (2:1) leading edge and spanned the full width of the wind tunnel test section.

The model tested in the wind tunnel was a 1/15th reduced scale drooped and scarfed short intake with a conical centrebody, representative of a modern Very High Bypass Ratio turbofan engine. The intake model was tested at fixed ground clearance of $h/D_{hi} = 0.3$, with h the vertical distance between the ground plane and the leading edge of the intake bottom lip and D_{hi} the intake highlight plane diameter.

B. Model Instrumentation and PIV Setup

The intake model was equipped with a total of 298 steady pressure sensors, 4 temperature sensors and 12 dynamic pressure sensors (Kulites). The total pressure distribution at the intake exit section (reference fan face plane) was measured using 8 equi-spaced radial rakes (every 45°) with 10 Pitot probes on each rake. 194 lip pressure taps were distributed streamwise around the lip at 10 different azimuthal locations.

Velocity measurements were taken using a multi-camera Stereoscopic Particle Image Velocimetry (S-PIV) optical set up consisting of 6 LaVision Imager sCMOS cameras with a sensor resolution of 2560 x 2160 px^2. Canon lenses were used with a focal length of 100mm. The cameras were positioned outside the test section to capture the entire intake model, which was illuminated by two Quantel Evergreen Nd:YAG lasers, mounted underneath the wind tunnel turntable floor (Fig. 3a and Fig. 3b). The flow was seeded with DEHS particles of 1 micrometer median diameter. PIV measurements with a velocity field acquisition frequency 15 Hz were taken at an Aerodynamic Interface Plane located -0.058D_i upstream of the intake exit section (reference fan face plane), with D_i intake inner diameter (Fig. 3c).

The PIV images were postprocessed using LaVision's DaVis 11 software for the calculation of the velocity fields. Each resulting PIV dataset consisted of a sequence of 1,000 snapshots obtained across a plane of size 250 x 250 mm^2. The final achieved spatial resolution was 1.5mm in both directions, which corresponded to a total of approximately 18,000 3-dimensional velocity vectors across the measurement plane. Only the data within $0.3R_{AIP} < r < 0.96R_{AIP}$ are used in the current analysis, in order to avoid spurious PIV data near the surfaces of the centrebody and the intake. Flow statistics were calculated using the 1,000 flow snapshots acquired per operating point.

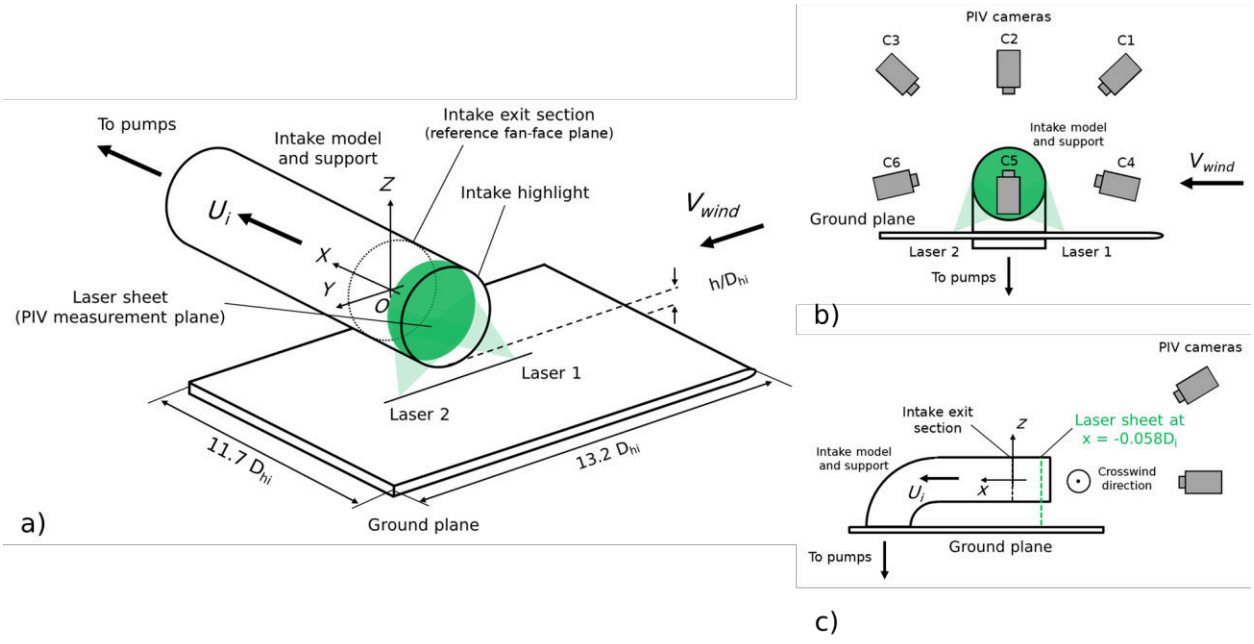

Fig. 3 Schematic of PIV set-up: a) schematic view of the test rig (intake and ground plane); b) PIV cameras set-up (front-view); c) PIV measurements on the vertical plane inside the intake.

C. Operating Conditions

The intake aerodynamics under crosswind conditions was investigated across a range of free steam velocity V_∞ and intake mass flow rate $\dot{m}$, primarily by varying the freestream velocity at a fixed value of mass flow through the intake and secondarily by varying the intake mass flow at a fixed crosswind velocity. The crosswind velocity was varied in the range between 2.5 kts and 43 kts. The intake Mass Flow Capture Ratio ($MFCR$, [31]):

$$MFCR = \frac{A_\infty}{A_{hi}} = \frac{\dot{m}}{\rho_\infty V_\infty A_{hi}} \tag{1}$$

was controlled by varying the intake mass flow rate, which was corrected as follows:

$$\tilde{m} = \dot{m} \frac{\sqrt{T_{0,\infty}/T_{ref}}}{P_{0,\infty}/P_{ref}} \tag{2}$$

where $T_{0\infty}$ is the tunnel total temperature, $P_{0,\infty}$ is the tunnel total pressure, T_{ref} is the ISA static temperature (288.15 K) and P_{ref} is the ISA static pressure (101,325 Pa). The flow conditions during the test were set as a percentage of a reference value $\tilde{m}_{ref}$, corresponding to the maximum mass flow rate inside the intake achievable by the suction pumps. The Reynolds number Re, defined in terms of the intake inner diameter D_i and freestream velocity V_∞ as follows:

$$Re = \frac{\rho_\infty V_\infty D_i}{\mu} \tag{3}$$

varied between $0.3 \cdot 10^5$ to $3.5 \cdot 10^5$. To prevent early laminar separation boundary layer trips were used on the outer side of the intake surface.

The test matrix of the flow conditions investigated is summarized by the intake performance map of Fig. 4, which classifies the intake operating points and the intake flow regimes as a function of crosswind velocity and $MFCR$.

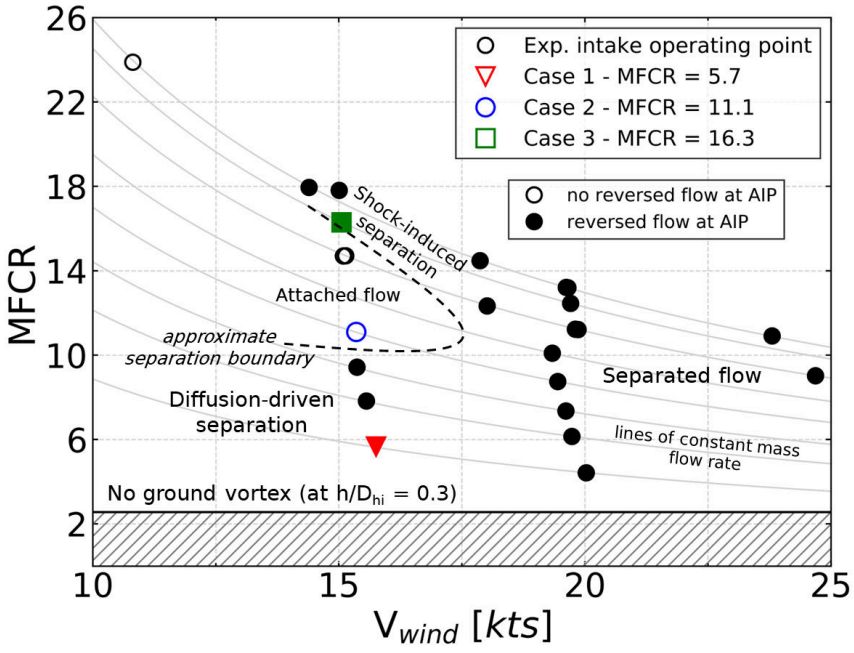

Fig. 4 Experimental intake performance map in crosswind.

The three operating points highlighted in Fig. 4, whose flow conditions are summarized in Table 1, will be discussed in the following. The ground clearance and the crosswind velocity, equal to 15 kts, are the same for the three cases, with the varying parameter being the intake mass flow rate, for a corresponding $MFCR$ increase from Case 1 to Case 3.

Table 1 Flow conditions for three different cases at 15 kts with increasing MFCR.

Case	h/D_{hi}	Crosswind velocity V_∞ [kts]	Intake mass flow rate $\widetilde{m}/\widetilde{m}_{ref}$ [%]	Mass Flow Capture Ratio $MFCR$	Reynolds number Re (10^6)
1	0.3	15	34%	5.7	0.127
2	-	-	65%	11.1	0.124
3	-	-	94%	16.3	0.121

D. Unsteady Swirl Distortion Evaluation

The analysis of the swirl distortion caused by flow non-uniformities was performed by means of the calculation at each acquired snapshot of a range of parameters derived from the industrial practice ([32]), evaluated with a ring and rake approach. The AIP was divided into a polar grid of 288 circumferential x 49 radial points equi-spaced circumferentially and with a radial spacing to provide an equal area distribution. The Delaunay triangulation method was used to interpolate the PIV data onto the grid points. The swirl descriptors were calculated based on the swirl angle distribution at a specific radial position. The swirl angle α is defined as the angle between the circumferential velocity and the axial direction velocity:

$$\alpha = tan^{-1}\left(\frac{v_\theta}{w}\right) \tag{4}$$

The swirl angle is considered positive in the clockwise direction and negative in the anticlockwise direction, forward-looking aft. The swirl angle distribution at each ring i was characterized by the Swirl Intensity SI, which represents the averaged absolute swirl angle and thus the magnitude of the swirl distortion, and Swirl Directivity SD, which represents the overall rotational direction of the swirling flow:

$$SI_i = \frac{SS_i^+\theta_i^+ + |SS_i^-|\theta_i^-}{360} \tag{5}$$

$$SD_i = \frac{SS_i^+\theta_i^+ + |SS_i^-|\theta_i^-}{SS_i^+\theta_i^+ + \left|SS_i^-\right|\theta_i^-} \tag{6}$$

where θ_i^+ and θ_i^- are positive and negative angle regions and $SS_i^+$and $SS_i^-$are positive and negative swirl sector elements. The overall Swirl Intensity $\overline{SI}$ and the overall Swirl Directivity $\overline{SD}$, corresponding to the average value on the plane, were defined as:

$$\overline{SI} = \frac{1}{N}\sum_{i=1}^{N}(SI)_i \tag{7}$$

$$\overline{SD} = \frac{1}{N}\sum_{i=1}^{N}(SD)_i \tag{8}$$

where N is the number of rings.

The conventional Swirl Coefficient based on the most distorted 60° sector $SC60$ ([33] and [34]) was also calculated to quantify the swirl distortion. The Swirl Coefficient $SC60$ is defined as the ratio of the maximum average circumferential velocity in a sector of 60° $|\overline{v_{\theta,60}}|$, to the area-averaged axial velocity at the AIP, $\overline{w_{AIP}}$:

$$SC60 = \frac{max\left(|\overline{v_{\theta,60}}|\right)}{\overline{w_{AIP}}} \tag{9}$$

The variations of the distortion parameters due to the unsteadiness in the flow were evaluated through the joint-probability density function maps of swirl descriptors introduced by Gil Prieto et al. [35]. The joint-PDF maps simultaneously illustrate the relationship between two distortion metrics for the entire set of snapshots acquired during the PIV measurements and highlight the probability of peak distortion events which a simple statistical analysis can fail to address. For the evaluation of the joint-PDF maps, the range of the descriptors was discretized into equi-spaced partitions and the probability was computed through the integration of the PDF on the descriptors grid, non-dimensionalized by the descriptor limits.

IV. Results and Discussion

A. Flow Field at the Aerodynamic Interface Plane

A first insight into the intake flow field topology can be obtained by plotting the time-averaged axial velocity at the Aerodynamic Interface Plane (AIP), normalized by the time-averaged area-averaged axial velocity $\langle \overline{w} \rangle_{AIP}$, which allows the identification of the region of reversed flow and the presence of the separation. The variation of the normalized axial velocity at the AIP plane for the three cases at 15 kts with increasing $MFCR$ is shown in Fig. 5.

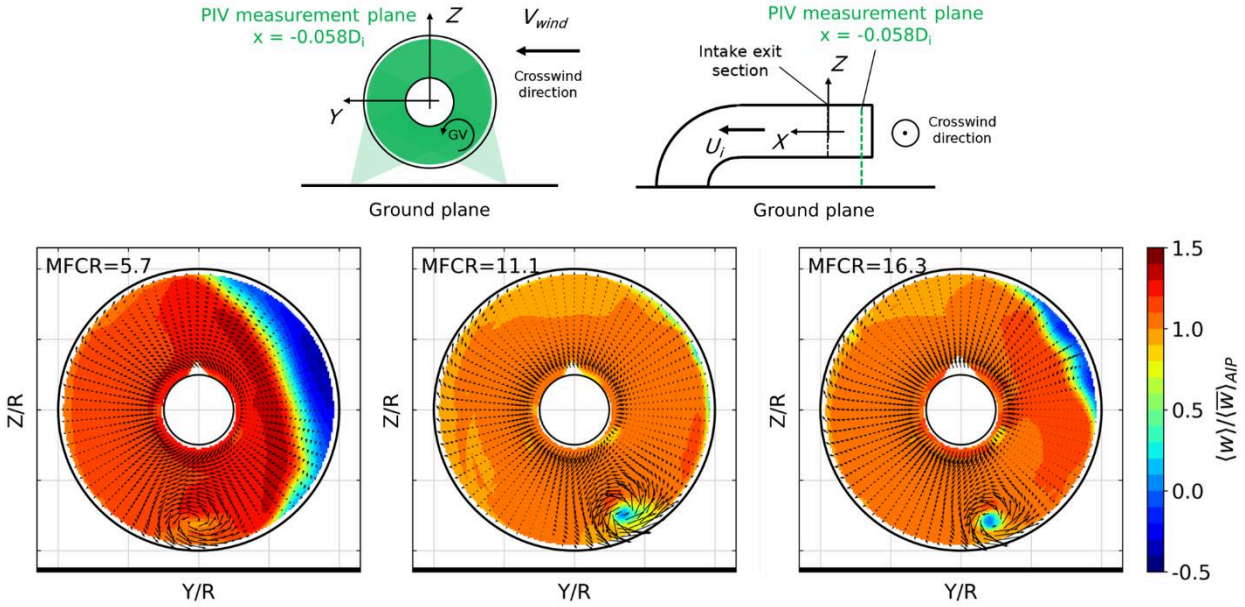

Fig. 5 PIV measured time-averaged non-dimensional axial velocity $\langle w \rangle / \langle \overline{w} \rangle_{AIP}$ at the AIP for cases 1 ($MFCR = 5.7$), 2 ($MFCR = 11.1$), and 3 ($MFCR = 16.3$) at 15kts.

As the $MFCR$ is increased, the intake flow goes from an initial separated condition ($MFCR = 5.7$, Case 1) to an attached condition ($MFCR = 11.1$, Case 2) and then separates again ($MFCR = 16.3$, Case 3). The non-axisymmetric geometrical features of the intake and the presence of the ground plane force the separation present in Case 1 and Case 3 into the top-half of the AIP on the windward side, with noticeably smaller radial and circumferential extent in Case 3 at high $MFCR$ with respect to Case 1 at low $MFCR$. Similar flow behavior, for which at a fixed crosswind velocity and increasing $MFCR$ two different separation mechanisms can be identified, is reported in previous experimental ([22] and [23]) and numerical studies ([26] and [27]). The isentropic Mach number distributions on the intake surface shown in Fig. 6 distinguish the different nature of the separation occurring in these cases. The contours of the time-averaged isentropic Mach number on the unwrapped surface of the intake in Fig. 6 derive from the linear interpolation of the static pressure tapping measurements onto the surface of the intake at the different azimuthal locations, with the axial coordinate normalized as such $x^* = (x - x_{hi})/L_i$, where x is the axial coordinate of each static pressure tap, x_{hi} is the highlight axial coordinate, and L_i is the length of the intake at the top-dead center. For Case 1 at $MFCR = 5.7$ (Fig. 6a) the distributions of isentropic Mach number present subsonic peak values all around the intake surface and the separation in this case is considered to be diffusion driven. At $MFCR = 11.1$ (Case 2) the time-averaged intake flow is still attached and mostly uniform (Fig. 5) and the isentropic Mach number distribution (Fig. 6b) presents values

approaching the sonic value, indicating a flow acceleration around the lip. At $MFCR = 16.3$ (Case 3), supersonic values in the isentropic Mach number distribution were found (Fig. 6c) and for this reason, the separation is expected to be shock-induced.

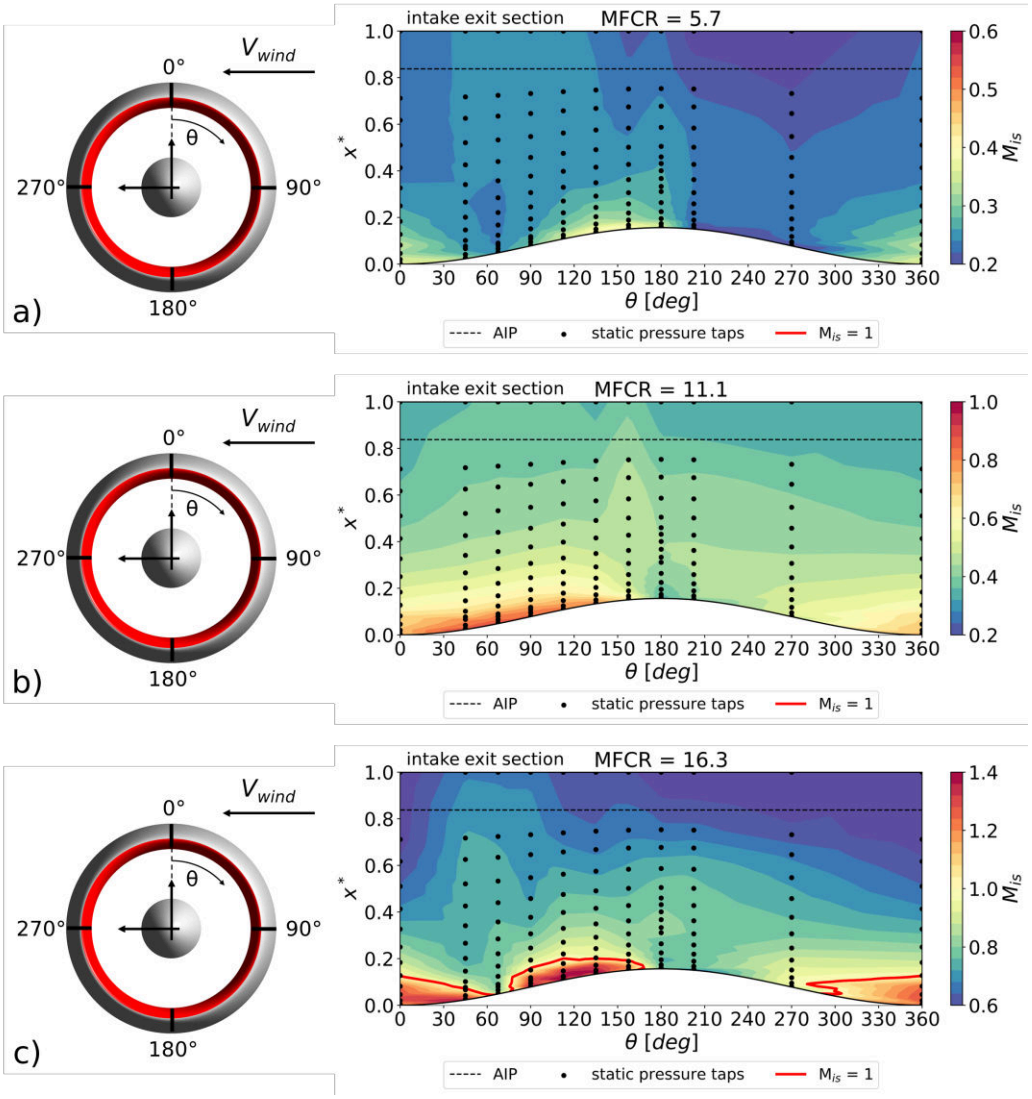

Fig. 6 Measured isentropic Mach number distributions around the intake surface: a) case 1 (diffusion-driven separation); b) case 2 (time-averaged attached intake flow); c) case 3 (shock-induced separation).

The non-dimensional time-averaged circumferential velocity $\langle v_\theta \rangle / \langle \overline{w} \rangle_{AIP}$, the non-dimensional time-averaged radial velocity $\langle v_r \rangle / \langle \overline{w} \rangle_{AIP}$ and the time-averaged swirl angle $\langle \alpha \rangle$ distributions were also calculated for the three configurations to examine the effect of the flow separation and of the ingested ground vortex on the flow field topology. The distributions of $\langle v_\theta \rangle / \langle \overline{w} \rangle_{AIP}$ for the three different $MFCR$s considered at 15kts are shown in Fig. 7. The maximum and minimum values are located in the lower part of the AIP around the area affected by the ingested ground vortex, responsible for an unsteady lateral oscillation of the flow. On the contrary, $\langle v_\theta \rangle / \langle \overline{w} \rangle_{AIP}$ is broadly unaffected by the intake flow separation which manifests as regions of reversed flow at the AIP in Case 1 $MFCR = 5.7$ and Case 3 at $MFCR = 16.3$.

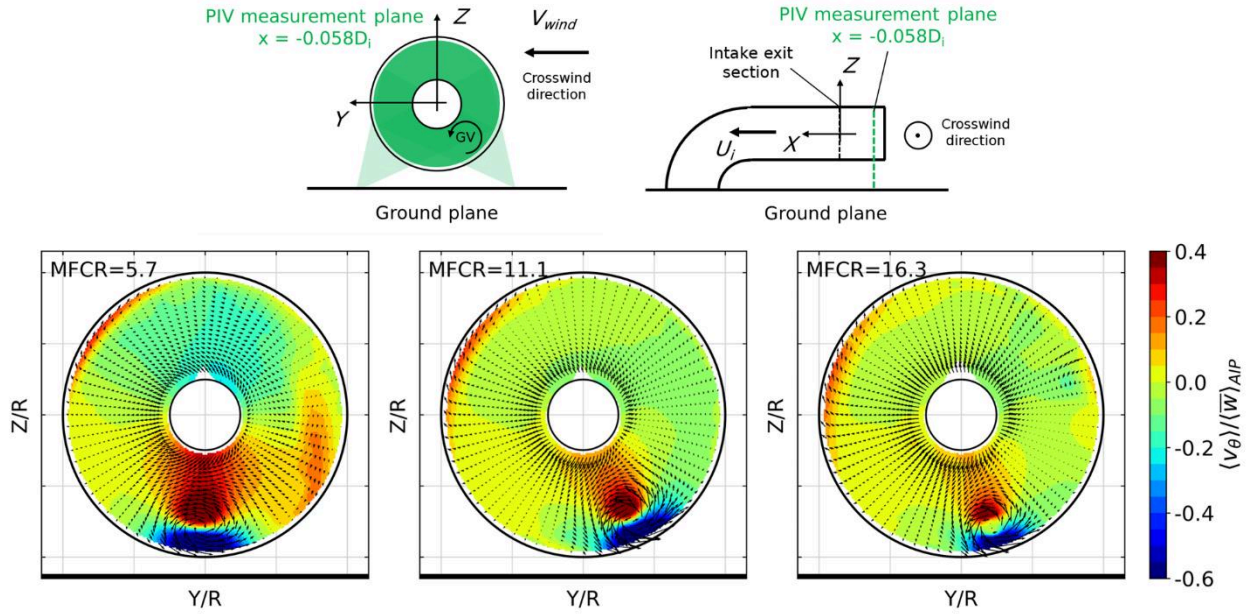

Fig. 7 Time-averaged non-dimensional circumferential velocity $\langle v_\theta \rangle / \langle \overline{w} \rangle_{AIP}$ at the AIP for cases 1 ($MFCR = 5.7$), 2 ($MFCR = 11.1$), and 3 ($MFCR = 16.3$) at 15kts.

The general topology of the non-dimensional time-averaged radial velocity $\langle v_r \rangle / \langle \overline{w} \rangle_{AIP}$ distributions (Fig. 8) shows that with increasing $MFCR$ the highest and lowest values of radial velocity are around the region of the ingested ground vortex, as similarly outlined for the circumferential velocity in Fig. 7. As emerged previously in Fig. 7 for the circumferential velocity, the radial velocity distribution is broadly unaffected by the presence of the separation (Case 1 at $MFCR = 5.7$ and Case 3 at $MFCR = 16.3$).

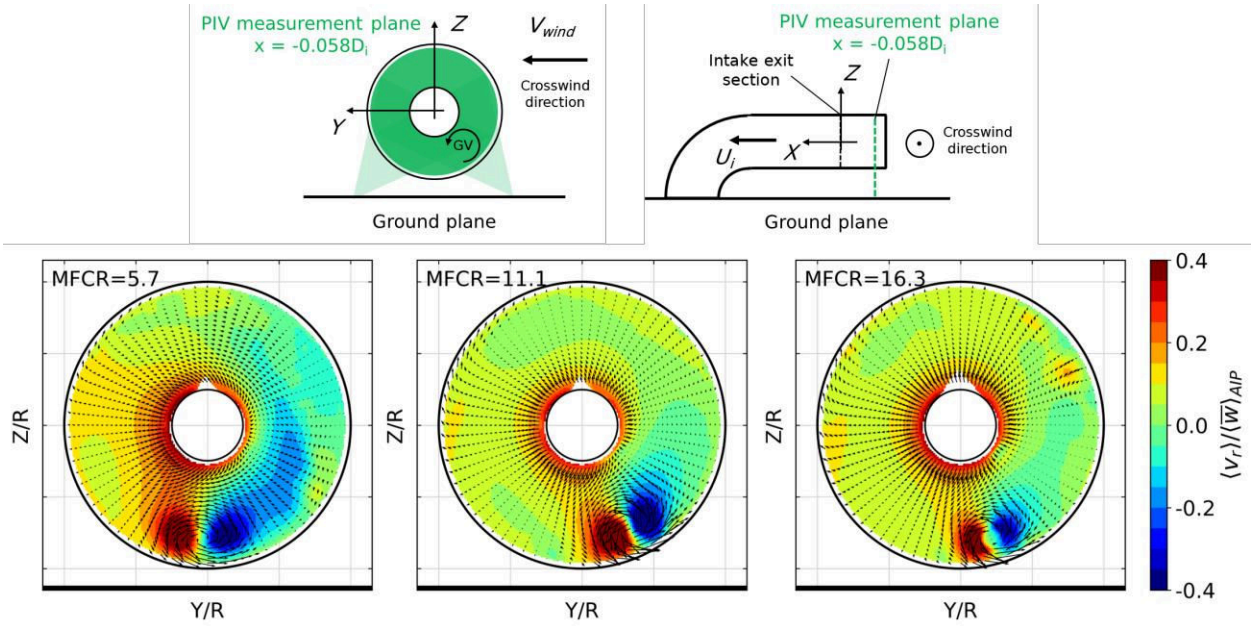

Fig. 8 Time-averaged non-dimensional radial velocity $\langle v_r \rangle / \langle \overline{w} \rangle_{AIP}$ at the AIP for cases 1 ($MFCR = 5.7$), 2 ($MFCR = 11.1$), and 3 ($MFCR = 16.3$) at 15kts.

The distributions of the time-averaged swirl angle (Fig. 9) show a different topology with increasing $MFCR$. For Case 2, corresponding to the attached configuration at $MFCR = 11.1$, the swirl angle distribution is primarily dominated by the circumferential velocity and the presence of the ingested ground vortex. For the higher value of $MFCR$ (Case 3, $MFCR = 16.3$) which corresponds to a shock-induced separation condition, the extent of the region affected by the ground vortex is reduced, along with the magnitude of the time-averaged swirl angle values. In this case, the separation on the windward side of the intake, apart being responsible for some localized region of high and low values of α on the top-half of the plane, has only a modest effect on the swirl angle distribution. This was somewhat expected, since the region of reversed flow caused by the shockwave at the intake lip is localized on the upper part of the AIP and is not very extensive (Fig. 5). The swirl angle distribution for the case at low $MFCR$ (Case 1, $MFCR = 5.7$), characterized by a diffusion-driven separation, is notably different to the one at $MFCR = 16.3$ (Case 3), presenting a much larger region of high swirl angle values, both positive and negative, roughly matching the extent of the reversed flow region identified in Fig. 5. Since the corresponding time-averaged circumferential velocity distribution of Fig. 7 does not present a significant level of circumferential velocity around the region encompassed by the separation, the increase of the swirl angle in the upper part of the AIP is therefore mainly due to the severity of the axial velocity deficit.

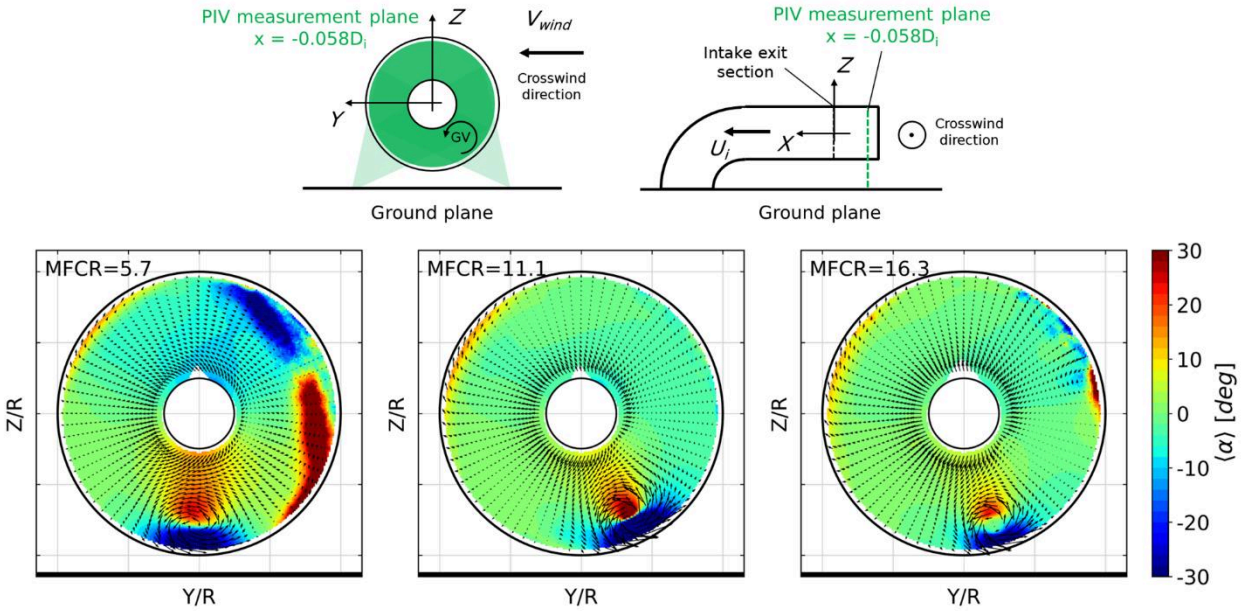

Fig. 9 Time-averaged swirl angle $\langle\alpha\rangle$ at the AIP for cases 1 ($MFCR = 5.7$), 2 ($MFCR = 11.1$), and 3 ($MFCR = 16.3$) at 15kts.

B. Unsteady Flow Analysis and Swirl Distortion Assessment

The high levels of time-averaged swirl angle and the presence of the separation at the AIP, highlighted in the previous section, are expected to negatively influence the performance of the intake, and worsen the operability of a notional downstream fan in a closely coupled system. A key aspect in the assessment of intake flow distortion is the quantification of the intensity of the fluctuations in the flow and the identification of the regions of the AIP more affected by the unsteadiness of the velocity field, which can be highlighted by considering the root mean square of the axial velocity fluctuations $w'_{RMS}/\langle\overline{w}\rangle_{AIP}$, shown in Fig. 10.

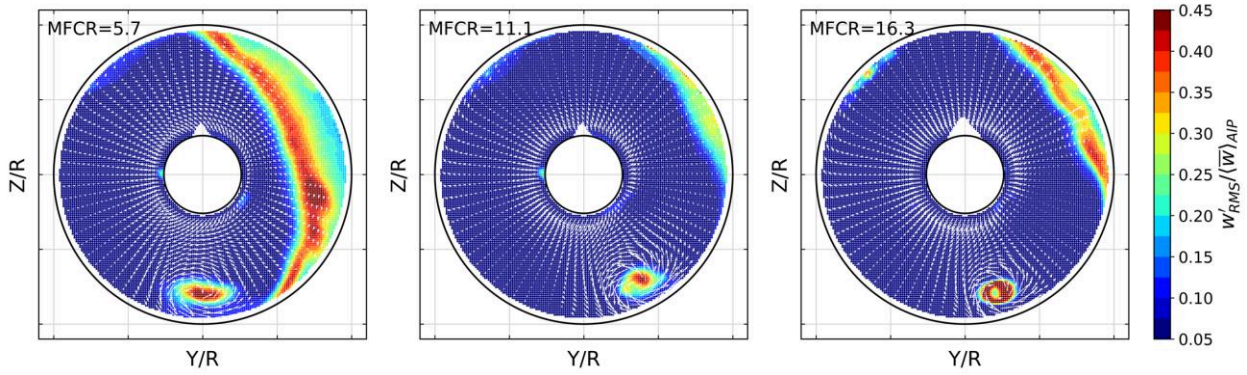

Fig. 10 Distributions of the non-dimensional out-of-plane velocity fluctuations $w'_{RMS}/\langle\overline{w}\rangle_{AIP}$, for cases 1 ($MFCR = 5.7$), 2 ($MFCR = 11.1$), and 3 ($MFCR = 16.3$) at 15kts.

For the lowest value of the $MFCR$ considered (Case 1, $MFCR = 5.7$), i.e. to the intake operating condition characterized by a diffusion-driven intake flow separation, the distribution of the root mean square of the out-of-plane velocity fluctuations presents an extensive region of peak unsteadiness corresponding to the separation, with a local maximum at the bottom of the separated region. Another local maximum of out-of-plane velocity fluctuations, with moderately wide horizontal extent, is located around the region occupied by the ingested ground vortex, indicative of high levels of unsteadiness in the flow. As the $MFCR$ is increased to $MFCR = 16.3$ (Case 3) the region of the highest unsteadiness corresponding to the shock-induced separation becomes less extensive, with peak values, although not notably reduced, located in the upper part of the AIP. This suggests that, as the $MFCR$ increases, the extent of the separated region reduces while the magnitude of the non-dimensional peak fluctuations broadly remains unchanged. The general flow topology highlighted in the time-averaged non-dimensional velocity distributions in Fig. 5 indicated that at $MFCR = 11.1$ (Case 2) the intake is attached, and the time-averaged flow is mostly uniform. However, the distribution of the velocity fluctuations in Fig. 10 shows evidence of a region of peak unsteadiness that can be linked to flow separation. The separation can be indeed identified by considering some sample non-dimensional instantaneous axial velocity distributions at the AIP in Fig. 11, which highlight the onset and decay of a region of reversed flow until reattachment, and the complexity of the flow field.

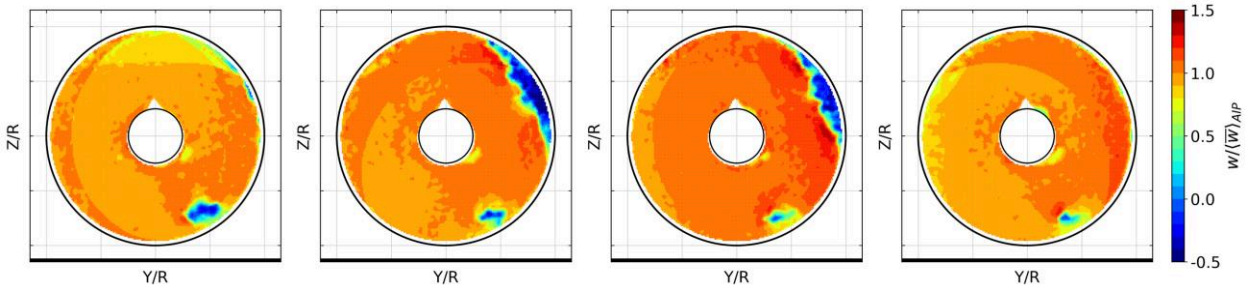

Fig. 11 Instantaneous axial velocity distributions at the AIP for case 2 ($MFCR = 11.1$) indicating the intake intermittent separation and reattachment.

Along with high fluctuations of the axial velocity component at the AIP due to onset of the lip separation, the flow field at the Aerodynamic Interface Plane also presents high levels of unsteadiness in swirl angle, as shown in Fig. 12. As the $MFCR$ is increased, high swirl regions characterized by high levels of unsteadiness are localized around the ground vortex core, especially at low $MFCR$ (Case 1, $MFCR = 5.7$), and in correspondence to the separation on the top-half of the intake, when present (Case 1 at $MFCR = 5.7$ and Case 3 at M$FCR = 16.3$). While the values across the rest of the AIP remain around zero, indicative of a mostly pure axial flow without any swirling component, the large region of reversed flow, even if only temporarily (Case 2, $MFCR = 11.1$), introduces extremely high peaks of swirl angle unsteadiness, indicative of huge spatial and temporal variations that are greater than the time-averaged values (Fig. 9).

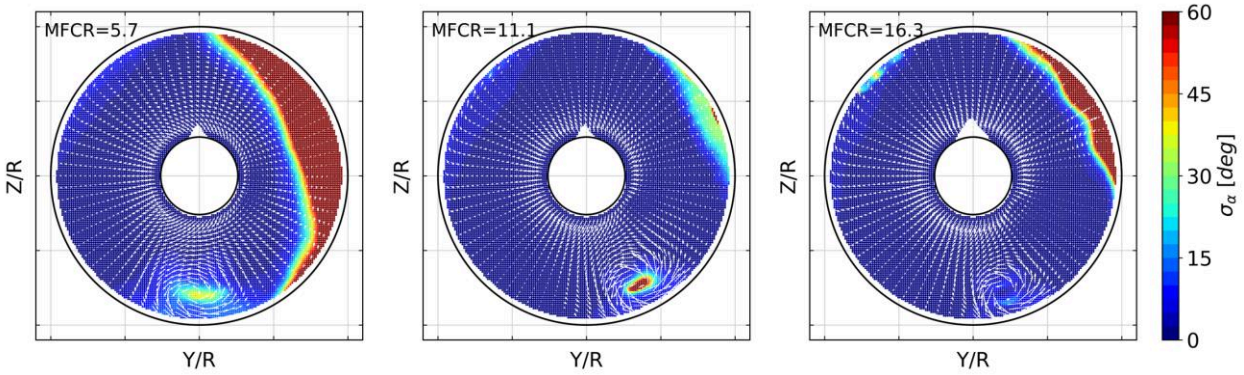

Fig. 12 Distributions of the swirl angle fluctuations σ_α, for cases 1 ($MFCR = 5.7$), 2 ($MFCR = 11.1$), and 3 ($MFCR = 16.3$) at 15kts.

As stated at the beginning of the current section, a key aspect in the assessment of the intake performance is the quantification of the unsteadiness of the separated flow fields around the time-averaged values. A consequential element in the analysis is the evaluation of the swirl distortion linked to the unsteadiness in the axial velocity and the swirl angle fields, to correlate the levels of distortion to the mechanisms of the separation. By considering the joint-PDF maps in terms of swirl coefficient and area-average swirl intensity (Fig. 13), the signature of the unsteady swirl descriptors depends on the $MFCR$ and the nature of the separation. Across the range of $MFCR$s from Case 1 to Case 3, the time-averaged and maximum swirl intensity is higher for the case where the diffusion-driven separation is present (Case 1, $MFCR = 5.7$, Fig. 13a), with respect to the time-averaged attached case (Case 2, $MFCR = 11.1$, Fig. 13b) and the case characterized by the shock-induced separation (Case 3, $MFCR = 16.3$, Fig. 13c). The characteristics of Case 2 at $MFCR = 11.1$ (Fig. 13b) are notable. The time averaged flow field is attached, and the swirl descriptors are considerably reduced compared with Case 1 at $MFCR = 5.7$ (Fig. 13a), which is strongly affected by the diffusion-driven separation. However, there are some isolated peak distortion events due to the instabilities associated with the instances of the flow in the intake being momentarily separated, as mentioned before, and shown in Fig. 11. This proves that the separation can produce high peaks of distortion that affect the intake performance and may cause distortion events notably different from the time-averaged values, in this case twice the time-averaged value. For Case 3 at $MFCR = 16.3$ the time averaged flow is separated due to a shock induced separation, but the swirl distortion levels are relatively low, roughly equal to the ones for Case 2 at $MFCR = 11.1$, presenting less scattered events, which is indicative of similarly relatively stable flow. This shows that separated cases at low $MFCR$s, characterized by diffusion-driven separation, can have a higher impact on the intake distortion and flow unsteadiness than separated cases at high $MFCR$s, where shock-induced separation is present. As the $MFCR$ is increased from Case 1 to Case 3, the swirl distortion in terms of $SC60$ presents a monotonically decreasing trend. While for the case with diffusion-driven separation (Case 1, $MFCR = 5.7$), the average and peak $SC60$ values are greater than those of the case with time-averaged attached flow at $MFCR = 11.1$ (Case 2), the statistical values of the swirl coefficient for the case characterized by shock-induced separation (Case 3, $MFCR = 16.3$), present even lower values compared to the ones for the attached cases. Considering that the $SC60$ parameter, as defined in Eq. 9, is an indicator of the level of the circumferential non-uniformities in the flow, this trend of the $SC60$ statistics suggests that the circumferential distortion is not primarily affected by the mechanisms of the separation, but by the presence of the ground vortex. Thus, it can be concluded that the $SC60$ may be not suitable for the characterization of highly separated intake flow.

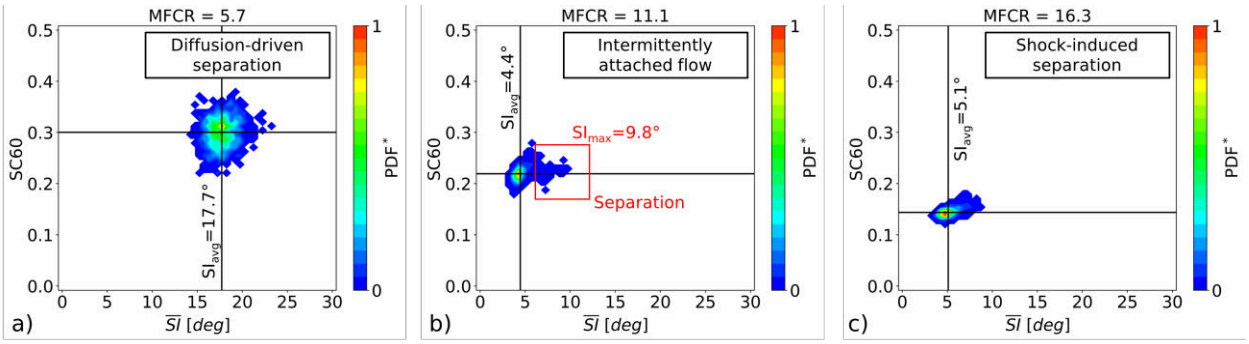

Fig. 13 $SC60$-$\overline{SI}$ j-PDF distributions at the AIP: a) Case 1 ($MFCR = 5.7$); b) Case 2 ($MFCR = 11.1$); c) Case 3 ($MFCR = 16.3$).

The high detrimental effect of the diffusion-driven separation on the performance of the intake in terms of swirl distortion is also reflected on the radial distribution of the swirl intensity across the AIP, as shown in Fig. 14. The average swirl intensity in each ring SI is plotted for each radial position, as a function of time and, correspondingly, of the PIV snapshot number. The scale of the color bars is different for better visualization. The diffusion-driven separated Case 1 at $MFCR = 5.7$ (Fig. 14a), affects a bigger portion of the AIP with respect to the shock-induced separation Case 3 at $MFCR = 16.3$ (Fig. 14c). The swirl distortion spans from the outer surface of the intake up to 70% of the AIP at $MFCR = 5.7$, with peak values above 40 deg, while for Case 3 characterized by shock-induced separation the peaks are notably reduced (between 15 and 20 deg) and the swirl distortion affects a smaller portion of the AIP plane (around 10%). Once more, the swirl distortion signature for Case 2, intermittently attached, is notable (Fig. 14b). Although separated only for less than 3s, the separation was found to spread from the outer surface up to 85% of the AIP radius, with peak values in the range between 15 and 30deg, which are visibly higher than the time-averaged values at the same radial positions.

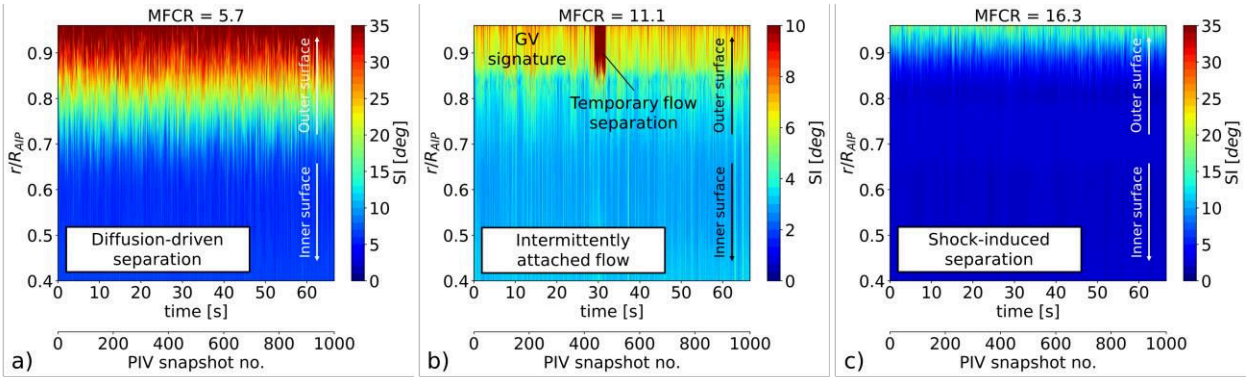

Fig. 14 Distributions of Swirl Intensity as a function of the AIP radius and time: a) Case 1 ($MFCR = 5.7$); b) Case 2 ($MFCR = 11.1$); c) Case 3 ($MFCR = 16.3$).

The swirl distortion caused by the different mechanisms of separation was proved to affect the AIP in as many ways, both in terms of radial extent and peak values. Considering the axial velocity and the swirl angle distribution at the AIP as a function of the $MFCR$ (Fig. 5 and Fig. 9), the key flow features present in an intake in crosswind can be illustrated in Fig. 15. High swirling flows can change the incidence angle of the fan and strongly affect the fan operability margin ([30]). Consequently, it is important to determine the direction of the swirling flow and the magnitude of the distortion at a radial position where the highest SI are observed, that is in the region encompassed by the ground vortex and the lip separation, close to the outer surface of the intake.

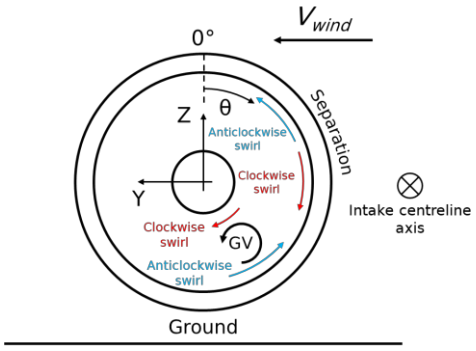

Fig. 15 Key swirl flow features in an intake operating in crosswind with ground vortex, with sign and coordinate frame of reference (view forward looking aft).

Considering one of the outer-most rings ($r/R_{AIP} = 0.92$), the SD-SI j-PDF maps for the three cases at increasing $MFCR$ (Fig. 16) show different patterns. For Case 1 at $MFCR = 5.7$, characterized by diffusion-driven separation, the j-PDF map at 92% of the AIP radius (Fig. 16a) presents a fairly equal distribution of swirl intensity both in the clockwise direction ($0 < SD < 1$) and in the anticlockwise direction ($-1 < SD < 0$), with high peak values above 45deg. This quasi-symmetric feature of the j-PDF map reflects the quasi-symmetric feature of the swirl angle distribution inside the reversed flow region, as shown in Fig. 9. For Case 3 at $MFCR = 16.3$, characterized by shock-induced separation, the j-PDF map in Fig. 16c presents a similar distribution to the one for the diffusion-driven separation, although the peak values of the swirl intensity are roughly halved, reflecting the fact that the shock-induced separation causes a less amount of swirl distortion with respect to the diffusion driven-separation, as discussed previously. It can be noted that the j-PDF map for Case 3 (Fig. 16c) is slightly biased towards the anticlockwise region (SD between -1 and 0), due to the contribution of the anticlockwise direction of the ground vortex at this radial position, as evident from the swirl angle distributions in Fig. 9. Once more, Case 2 at $MFCR = 11.1$, characterized by a temporary separation, is notable. In the SD-SI j-PDF map for this case (Fig. 16b, the anticlockwise swirl component is predominant, due to fact that at this radial location the ground vortex is introducing a negative circumferential distortion in the flow. As a consequence, an increased blade loading due to an increase in incidence would be observed at the regions in the vicinity of the tip of a notional fan rotor, with a possible reduction in the stability margin ([30]). However, the operability reductions cannot be quantified with the present analysis as no rotor was in place during these tests and more importantly because no velocity data is available for radii beyond 96% of the AIP hence no operability analysis across a full blade span can be made. Although the j-PDF map for Case 3 (Fig. 16c) presents a fairly clustered distribution with an average SI value below 10deg, the presence of a intermittent flow separation is responsible for peak events of above 15deg, with a maximum close to 30deg. The peak events are scattered both in the clockwise and in the anticlockwise region of the map, reflecting the fact that the combined unsteadiness of the separation and the ground vortex causes the direction of the swirl distortion to be dominant in one direction, in the other, or to be roughly balanced. This shows that even if the separation is only intermittent, the amount of swirl distortion introduced in the flow can worsen the performance of the intake and can negatively affect the downstream compression system operability and performance.

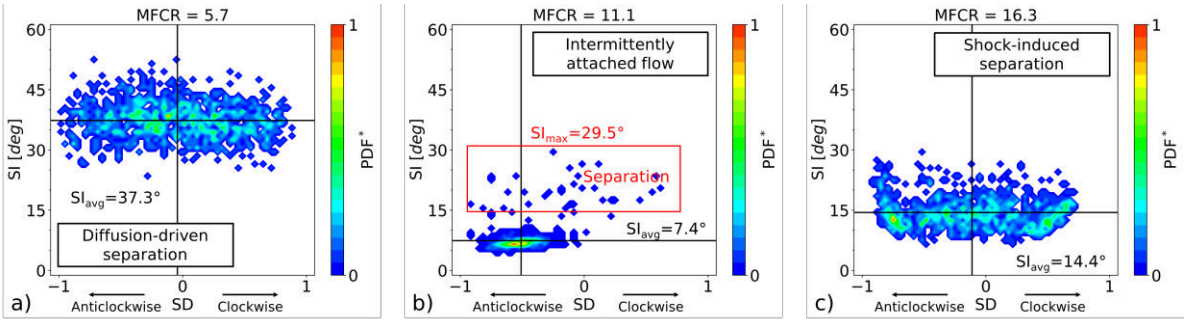

Fig. 16 SD-SI j-PDF distributions evaluated at $r/R_{AIP} = 0.92$: a) Case 1 ($MFCR = 5.7$); b) Case 2 ($MFCR = 11.1$); c) Case 3 ($MFCR = 16.3$).

V. Conclusion

In this study, the analysis of PIV data for a short intake operating under crosswind conditions was performed. The high spatial resolution and time-variant data gathered during the PIV experiments allowed the characterization of the swirl distortion inside the intake caused by the ground vortex and the intake separation with a level of detail that has never been seen before. The non-dimensional time-averaged velocity fields at the AIP combined with the static pressure distributions on the intake surface were used to classify the intake operating regime and identify the presence of flow separation associated with either diffusion or the occurrence of a shockwave. The two different separation mechanisms were found to be responsible for different levels of variations in the axial velocity and swirl angle. The results showed that the level of circumferential distortion is mainly associated with the ground vortex, while the amount of swirl distortion is mainly dependent on the severity of the intake separation. Of the three cases considered at a fixed crosswind velocity and increasing $MFCR$, the operating point characterized by diffusion-driven separation presented higher values of fluctuations on a wider area of the AIP with respect to the one characterized by shock-induced separation. Intermittent separation inside the intake was found to be responsible for peak swirl distortion values twice the magnitude of the time-averaged ones at a medium $MFCR$ operating point. When only the ground vortex is present, the most intense swirl distortion events in terms of swirl intensity are associated with an anticlockwise swirl, with swirl intensity values relatively lower compared to those associated with the lip separation. The high-swirl events associated with both the ground vortex and the lip separation could adversely affect the stability of the engine and needs to be considered for the intake-engine performance assessment.

Acknowledgments

This work was conducted under the NIFTI project which received funding from the Clean Sky 2 Joint Undertaking (JU) under Grant Agreement No 866521. The authors would like to thank German-Dutch Wind Tunnels (DNW) and LaVision GmbH for generating and providing the velocity data used in this study as part of the NIFTI project.

References

[1] Birch, N. T., "2020 Vision: The Prospects for Large Civil Aircraft Propulsion," The Aeronautical Journal, Vol. 104, No. 1038, 2000, pp. 347–352. https://doi.org/10.1017/S0001924000063971

[2] Hughes, C., Van Zante, D., and Heidmann, J., "Aircraft Engine Technology for Green Aviation to Reduce Fuel Burn," 2011. https://doi.org/10.2514/6.2011-3531

[3] Owens, R., Hasel, K., and Mapes, D., "Ultra High Bypass Turbofan Technologies for the Twenty-First Century," 1990. https://doi.org/10.2514/6.1990-2397

[4] Boscagli, L., Christie, R., MacManus, D., and Piovesan, T., "Aerodynamics of a Short Intake in Crosswind," Aerospace Science and Technology, Vol. 129, 2022, p. 107826. https://doi.org/10.1016/j.ast.2022.107826

[5] Siervi, F. De, Viguier, H. C., Greitzer, E. M., and Tan, C. S., "Mechanisms of Inlet-Vortex Formation," Journal of Fluid Mechanics, Vol. 124, No. 1, 1982, p. 173. https://doi.org/10.1017/S0022112082002456

[6] Shin, H. W., Cheng, W. K., Greitzer, E. M., and Tan, C. S., "Inlet Vortex Formation Due to Ambient Vorticity Intensification," AIAA Journal, Vol. 24, No. 4, 1986, pp. 687–689. https://doi.org/10.2514/3.9330

[7] Shin, H. W., Greitzer, E. M., Cheng, W. K., Tan, C. S., and Shippee, C. L., "Circulation Measurements and Vortical Structure in an Inlet-Vortex Flow Field," Journal of Fluid Mechanics, Vol. 162, No. 1, 1986, p. 463. https://doi.org/10.1017/S0022112086002124

[8] Liu, W., Greitzer, E. M., and Tan, C. S., "Surface Static Pressures in an Inlet Vortex Flow Field," Journal of Engineering for Gas Turbines and Power, Vol. 107, No. 2, 1985, pp. 387–393. https://doi.org/10.1115/1.3239738

[9] Nakayama, A., and Jones, J. R., "Correlation for Formation of Inlet Vortex," AIAA Journal, Vol. 37, No. 4, 1999, pp. 508–510. https://doi.org/10.2514/2.743

[10] Brix, S., Neuwerth, G., and Jacob, D., "The Inlet-Vortex System of Jet Engines Operating near the Ground," 2000. https://doi.org/10.2514/6.2000-3998

[11] Murphy, J. P., and MacManus, D. G., "Ground Vortex Aerodynamics under Crosswind Conditions," Experiments in Fluids, Vol. 50, No. 1, 2011, pp. 109–124. https://doi.org/10.1007/s00348-010-0902-4

[12] Wang, Z., and Gursul, I., "Unsteady Characteristics of Inlet Vortices," Experiments in Fluids, Vol. 53, No. 4, 2012, pp. 1015–1032. https://doi.org/10.1007/s00348-012-1340-2

[13] Boldman, D., Iek, C., Hwang, D., Larkin, M., and Schweigher, P., "Effect of a Rotating Propeller on the Separation Angle of Attack," 1993. https://doi.org/10.2514/6.1993-17

[14] Motycka, D. L., "Reynolds Number and Fan/Inlet Coupling Effects on Subsonic Transportinlet Distortion," Journal of Propulsion and Power, Vol. 1, No. 3, 1985, pp. 229–234. https://doi.org/10.2514/3.22785

[15] Larkin, M. J., and Schweiger, P. S., "Ultra High Bypass Nacelle Aerodynamics," No. NASA CR-189149, 1992.

[16] Schulze, S., Kähler, C., and Radespiel, R., "On Stalling Flow-Through Nacelles and Powered Inlets at Take-Off Conditions," 2008. https://doi.org/10.2514/6.2008-789

[17] Schulze, S., and Kaehler, C. J., "Analysis of the Flow in Stalling Engine Inlet Models with Different Visualization and Measurement Techniques," Second Symposium "Simulation of Wing and Nacelle Stall", 2010, pp. 1–12.
[18] Probst, A., Schulze, S., Radespiel, R., and Kähler, C. J., "Numerical and Experimental Investigation of a Stalling Flow-Through Nacelle," Notes on Numerical Fluid Mechanics and Multidisciplinary Design, Vol. 112, 2010, pp. 537–544. https://doi.org/10.1007/978-3-642-14243-7_66
[19] Probst, A., Schulze, S., Kähler, C. J., and Radespiel, R., "Reynolds-Stress Modelling of Subsonic and Transonic Inlet Stall Compared to Measurements," Third Symposium "Simulation of Wing and Nacelle Stall", Braunschweig, 21. - 22. June 2012, pp. 1–13.
[20] Probst, A., Schulze, S., Radespiel, R., and Kähler, C. J., "Numerical Simulation of Engine-Inlet Stall with Advanced Physical Modelling Compared to Validation Experiments," Notes on Numerical Fluid Mechanics and Multidisciplinary Design, Vol. 121, 2013, pp. 565–573. https://doi.org/10.1007/978-3-642-35680-3_67
[21] Kennedy, S., Robinson, T., Spence, S., and Richardson, J., "Computational Investigation of Inlet Distortion at High Angles of Attack," Journal of Aircraft, Vol. 51, No. 2, 2014, pp. 361–376. https://doi.org/10.2514/1.C031789
[22] Quémard, C., Garçon, F., and Raynal, J., "High Reynolds number air intake tests in the ONERA F1 and S1MA wind tunnels," Workshop on airframe engine integration at DLR, DLR, Mar. 1996, Braunschweig, France.
[23] Lecordix J., Mullender A., Lecossais E., Godard J., and Hepperle M., "Hybrid laminar flow nacelle design," ICAS Proceedings. 20: 504–520.
[24] Hall, C., and Hynes, T., "Measurements of Intake Separation Hysteresis in a Model Fan and Nacelle Rig," Vol. 22, 2002. https://doi.org/10.2514/6.2002-3772
[25] Hall, C., and Hynes, T., "Nacelle Interaction with Natural Wind Prior to Take-Off," Vol. 21, 2002. https://doi.org/10.2514/6.2002-3773
[26] Colin Y., Aupoix B., Boussuge J.-F., and Chanez, P., "Numerical Simulation and Analysis of Crosswind Inlet Flows at Low Mach numbers," 8th International Symposium on Experimental and Computational Aerothermodynamics of Internal Flows Lyon, Jul 2007, Lyon, France.
[27] Zhang, M., "Numerical Investigation of Nacelle Intake Flow Distortion at Crosswind Conditions," 32nd Congress of the International Council of the Aeronautical Sciences, ICAS 2021, 2021, pp. 1–11.
[28] Harjes, L., Bode, C., Grubert, J., Frantzheld, P., Koch, P., and Friedrichs, J., "Investigations of Jet Engine Intake Distortions Caused by Crosswind Conditions," Journal of the Global Power and Propulsion Society, Vol. 4, 2020, pp. 48–62. https://doi.org/10.33737/jgpps/118875
[29] Freeman, C., and Rowe, A. L., "Intake Engine Interactions of a Modern Large Turbofan Engine," Vol. m, 1999, pp. 3–8. https://doi.org/10.1115/99-GT-344
[30] "A Methodology for Assessing Inlet Swirl Distortion," Society of Automotive Engineers, SAE Aerospace Information Report 5686, 2022.
[31] Seddon, J., and Goldsmith, E., "Intake Aerodynamics, Second Edition," American Institute of Aeronautics and Astronautics, Inc., Washington, DC, 1999. https://doi.org/10.2514/4.473616
[32] Bouldin, B., and Sheoran, Y., "Inlet Flow Angularity Descriptors Proposed for Use With Gas Turbine Engines," 2002. https://doi.org/10.4271/2002-01-2919
[33] Guo, R. W., and Seddon, J., "The Swirl in an S-Duct of Typical Air Intake Proportions," Aeronautical Quarterly, Vol. 34, No. 2, 1983, pp. 99–129. https://doi.org/10.1017/S0001925900009641
[34] Guo, R. W., and Seddon, J., "Swirl Characteristics of an S-Shaped Air Intake with Both Horizontal and Vertical Offsets," Aeronautical Quarterly, Vol. 34, No. 2, 1983, pp. 130–146. https://doi.org/10.1017/S0001925900009653
[35] Gil-Prieto, D., Zachos, P., MacManus, D. G., and Tanguy, G., "Convoluted Intake Distortion Measurements Using Stereo Particle Image Velocimetry," 2016. https://doi.org/10.2514/6.2016-3560

2024-01-04

Unsteady swirl distortion in a short intake under crosswind conditions

Piovesan, Tommaso

AIAA

Piovesan T, Zachos PK, MacManus DG, Sheaf C. (2024) Unsteady swirl distortion in a short intake under crosswind conditions. In: AIAA SCITECH 2024 Forum, 8-12 January 2024, Orlando, USA. Paper number AIAA 2024-1384

https://doi.org/10.2514/6.2024-1384